



**HAL**  
open science

# Correcting the side effects of ADC filtering in MR image reconstruction

Carole Lazarus, Maximilian März, Pierre Weiss

► **To cite this version:**

Carole Lazarus, Maximilian März, Pierre Weiss. Correcting the side effects of ADC filtering in MR image reconstruction. 2018. hal-01817643v1

**HAL Id: hal-01817643**

**<https://hal.science/hal-01817643v1>**

Preprint submitted on 18 Jun 2018 (v1), last revised 14 May 2020 (v2)

**HAL** is a multi-disciplinary open access archive for the deposit and dissemination of scientific research documents, whether they are published or not. The documents may come from teaching and research institutions in France or abroad, or from public or private research centers.

L'archive ouverte pluridisciplinaire **HAL**, est destinée au dépôt et à la diffusion de documents scientifiques de niveau recherche, publiés ou non, émanant des établissements d'enseignement et de recherche français ou étrangers, des laboratoires publics ou privés.

# Correcting the side effects of ADC filtering in MR image reconstruction

Carole Lazarus, Maximilian März & Pierre Weiss

June 18, 2018

## Abstract

This work investigates the role of the filters implemented on modern ADCs for the reconstruction of magnetic resonance images. We analyze both from a theoretical and experimental point of view the effects of these filters and demonstrate how it may lead to severe degradation of the reconstructed images when using modern sampling patterns. Based on these findings, we propose a mathematical model and a numerical algorithm that allow to mitigate such filtering effects. Experiments on simulated and real data on a 7 Tesla scanner show that the proposed ideas allow to drastically improve the overall image quality.

## 1 Introduction

The standard acquisition model in MRI states that the continuous Fourier transform of an image  $u : \Omega \rightarrow \mathbb{C}$  is sampled on a set of discrete points in what is commonly called the  $k$ -space. The space  $\Omega \subset \mathbb{R}^d$  is the field of view, with  $d = 2$  or  $d = 3$  denoting the space dimension. The particularity of MRI is that these samples are measured along several parametrized curves  $\lambda : [0, T] \mapsto \mathbb{R}^d$ , called  $k$ -space trajectories or shots. According to this model, given a sampling period  $\Delta t$  and letting  $\hat{u}$  denote the Fourier transform of the image  $u$ , the measured samples are modeled as [12]:

$$y_j = \hat{u}(\lambda(j\Delta t)), \quad (1)$$

where  $j \in \mathbb{N}$  denotes the index of the measurement. Most commonly, these points lie on a grid, which is filled by parallel Cartesian lines [18], but non-Cartesian sampling such as spiral trajectories [24] may also be used for their greater sampling efficiency and are becoming increasingly popular with the advent of compressed sensing [21].

Nevertheless, the model expressed in equation (1) does not account for the analog-to-digital converter (ADC), which converts the continuous signal  $f(t) = \hat{u}(\lambda(t))$  into discrete values. The model that will be used to describe

this effect is a linear time invariant filter of the type:

$$y_j = (h \star f)(j\Delta t), \quad (2)$$

where  $\star$  denotes a convolution operator and  $h$  is a filter that depends on the ADC technology. The main point of this article is to show that neglecting the filtering effect in model (2) can have a dramatic impact on the reconstruction quality and to propose numerical algorithms to handle it. We will give a particular attention to two typical situations: a simple integrator ADC and more advanced bandlimiting filters which are typically used in modern MRI scanners.

- **Integration effect.** The earliest ADCs were simply integrating ADCs, meaning that the ADC simply *integrates* the Fourier transform  $\hat{u}$  over a the  $k$ -space path. This model reads as  $y_j = \int_{(j-1)\Delta t}^{j\Delta t} \hat{u}(\lambda(t)) dt$  and can be cast into equation (2) by choosing  $h = \mathbb{1}_{[0, \Delta t]}$ . The interest of choosing a large sampling period  $\Delta t$  is that the signal-to-noise ratio (SNR) increases since more signal is averaged over time [15], which is a typical reasoning in MRI physics. We will see later that this improvement might not compensate the downsides that come along with it.
- **Bandlimiting filtering.** On most MR scanners, the ADC bandwidth is fixed and much higher than the desired receiver bandwidth [2]. The ADC rate reaches several megahertz, while the receiver bandwidth usually ranges from about 5 to 100 kHz [13]. To produce the measurements at the desired sampling rate, bandlimiting filtering is applied on the digitized data before decimation. This bandlimiting step is introduced both to avoid aliasing of the temporal signal  $f$  when subsampling it and to reduce the noise. A perfect bandlimiting filter takes the form  $h(t) = \text{sinc}(t/\Delta t)$ .

To the best of our knowledge, the effects of ADC filtering on image reconstructions have not yet been described or studied in the literature.

The higher complexity of the model may be a possible explanation for this omission, since equation (2) no longer represents a Fourier transform, preventing a straightforward application of standard tools such as the fast Fourier transform. Furthermore, this effect might go unnoticed when using standard Cartesian acquisitions which are usually oversampled by a factor of 2 in the readout direction compared to the Nyquist rate. We will see later that the classical model in that case is sufficient to reconstruct high quality images. However, in situations where faster trajectories are used, as is the case of spiral sampling and/or when the use of oversampling is not possible due to low signal-to-noise-ratio (SNR), significant artifacts may appear.

In section 2, we first show how the classical approximation in equation (1) can lead to detrimental artifacts in the reconstructed images, even in the case of Cartesian sampling at Nyquist rate. Depending on the trajectories, intensity modulations, space-varying blurs and image deformations can be observed when ignoring ADC filtering.

In many situations, the filter  $h$  is not provided by the manufacturer and correcting the effect hence requires its estimation. In section 3, we propose a reverse engineering technique based on the design of specific sequences and numerical algorithms to estimate the applied filter  $h$ .

In section 4, we propose numerical algorithms to handle the ADC filtering effect for linear and nonlinear reconstructions methods. These are based on a combination of numerical integration methods and of the nonuniform Fast Fourier transform.

In section 5, the proposed algorithms are tested against simulated and real data, showing significant improvements in the reconstruction quality, especially when using the novel trajectories designed in the framework of compressed sensing.

## 1.1 Notation

In this paper, we assume that the image domain is  $\Omega = [-1/2, 1/2]^2$ . We chose to work in 2D to simplify the exposition, but an extension to 3D is direct. Similarly, the domain can be shifted and inflated to account for a different field of view with straightforward scaling arguments. Notice that with the choice  $\Omega = [-1/2, 1/2]^2$ , Shannon's sampling theorem [27] suggests to take samples on a Cartesian grid, with a grid size of length 1.

The space  $L^2(\Omega)$  is defined as the set of measurable functions  $u$  with finite  $L^2$  norm, i.e.  $\|u\|_{L^2}^2 := \int_{\Omega} |u|^2(x) dx < +\infty$ . The canonical Hermitian product on  $\mathbb{C}^n$  and  $L^2(\Omega)$  is denoted  $\langle \cdot, \cdot \rangle$ . Let  $u : \Omega \rightarrow \mathbb{C}$  denote a magnetic resonance image in  $L^2(\Omega)$ . Its Fourier

transform is defined for all  $\xi \in \mathbb{R}^2$  by:

$$\hat{u}(\xi) = \int_{\Omega} \exp(-2i\pi \langle x, \xi \rangle) u(x) dx.$$

The Dirac delta function at 0 is denoted by  $\delta$  and the Dirac delta function at a position  $x$  is denoted  $\delta_x$ .

Given two functions  $f$  and  $g$ , the tensor product of  $f$  and  $g$  is defined by  $(f \otimes g)(x, y) = f(x)g(y)$  for all  $x, y$ . We recall that the Fourier transform preserves the tensor form:  $\mathcal{F}(f \otimes g) = \mathcal{F}(f) \otimes \mathcal{F}(g)$ .

## 2 The deleterious consequences of filtering

The aim of this section is to explain the ADC filtering effects on the reconstruction of signals and when it is important to account for them. We start by the simple case of Cartesian trajectories and then turn to more general sampling patterns.

### 2.1 The case of Cartesian sampling

The filtering effect in the case of Cartesian sampling with constant speed  $s$  can be understood by an analytical argumentation. In that case, for each sampling point, the filtering is performed along the readout direction only. A convenient way to formalize this observation is to introduce the following tensor product filter  $\hat{\mu} = g \otimes \delta$ , where  $g(t) = h(t/s)$  and to observe that the acquisition model can then be written as:

$$y_{i,j} = (\hat{u} \star \hat{\mu})(i\Delta\xi, j\Delta\xi) \quad (3)$$

where  $(i, j) \in \{-n/2, n/2 - 1\}^2$  describe the set of samples indices, and  $n \in \mathbb{N}$  describes the number of samples in each  $k$ -space direction.

Now, by not accounting for the filtering effect, the best we can hope for is to reconstruct an image  $u^*$  of the form  $u^* = \mathcal{F}^{-1}(\hat{u} \star \hat{\mu}) = u \cdot \mu$ , where  $\mu$  is defined by:

$$\mu = \mathcal{F}^{-1}(g \otimes \delta) = \mathcal{F}^{-1}(g) \otimes \mathcal{F}^{-1}(\delta) = \mathcal{F}^{-1}(g) \otimes \mathbb{1}.$$

Depending on the filter  $h$ , different effects can be expected.

**Integration** In the case of an integration filter, we have  $h = \mathbb{1}_{[0, \Delta t]}$ , where  $\Delta t$  is the sampling period. Then  $g = \mathbb{1}_{[0, \Delta \xi]}$ , where  $\Delta \xi = s\Delta t$  is the length of the segment over which the Fourier transform is integrated. Hence,  $\mathcal{F}^{-1}(g)$  is a sinc filter, and the filtering effect hence produces an image modulated by

a sinc. Depending on the integration length  $\Delta\xi$ , this effect will either just lower the contrast at the image boundaries, or create low frequency oscillations.

**Sinc** By using a sampling period  $\Delta t$ , the standard Shannon-Nyquist sampling theorem states that it is impossible to reconstruct frequencies beyond the interval  $I = [-\frac{1}{2\Delta t}, \frac{1}{2\Delta t}]$ . Hence, to avoid aliasing effects, one may be tempted to use a perfect bandlimiting filter of the type  $\hat{h} = \mathbb{1}_I$ . In that case, we would get  $h(t) = \text{sinc}(\frac{t}{\Delta t})$ . The filtering effect in that case would simply crop the image in one direction on the interval  $I$ .

We now propose to simulate the effect using 4 different Cartesian sequences with  $\Delta\xi \in \{\frac{1}{2}, 1, 2, 4\}$ . The value  $\Delta\xi = 1/2$  corresponds to the most standard Cartesian trajectory in MRI (oversampling factor of 2 along the readout direction). The value  $\Delta\xi = 1$  corresponds exactly to the Shannon's limit sampling rate for an image supported on  $[-1/2, 1/2]^2$ . For the simulation, our measurements are created by incorporating the filtering effect as expressed in equation (3). For example, in the integration case with  $\Delta\xi = 2$ , each sample results from the integration of two consecutive samples acquired at  $\Delta\xi = 1$ . The reconstruction algorithm is based on a standard inverse discrete Fourier transform (which does not account for any filtering effects). Fig. 1 and 2 show the results for the integration and the sinc filtering respectively as well with a cross section of the images. The modulation due to the integration filtering can be seen on the cross sections for all values of  $\Delta\xi$ . On the contrary, the effect of the sinc filtering can be seen only for  $\Delta\xi \in \{2, 4\}$ , with a dramatic effect: the disk is cropped with an irreversible loss of information.

Overall this experiment highlights the fact that larger distances between consecutive samples in the  $k$ -space result in a more pronounced filtering effect.

## 2.2 The case of arbitrary trajectories

For more general trajectories, it seems hard to give an analytical description of the filtering effects. From a mathematical viewpoint, it amounts to studying integral operators with kernels defined as measures supported on one dimensional curves. To the best of our knowledge, very little is currently known for such operators. Hence we restrict ourselves to provide experimental simulations with spiral trajectories, which are one of the most widespread non-Cartesian trajectories.

Fig. 3 shows a sampling pattern made of 200 interleaved spirals, which were designed using the method proposed in [20]. Each spiral is depicted with a different color going continuously from blue to green. The number

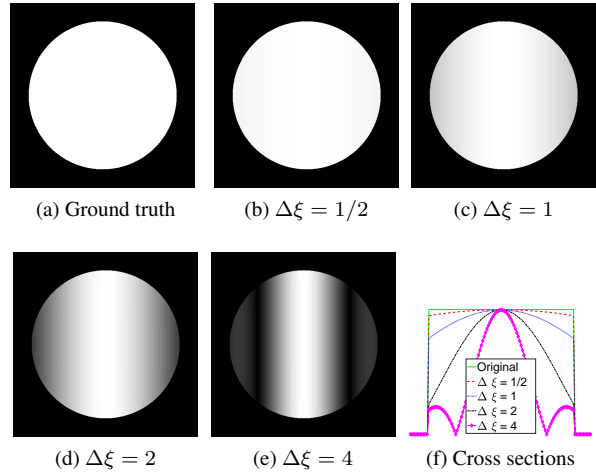


Figure 1: The integration effect with a Cartesian sampling. Note: the images might be complex valued, and we only display their modulus. This explains why negative oscillations are seen as positive values.

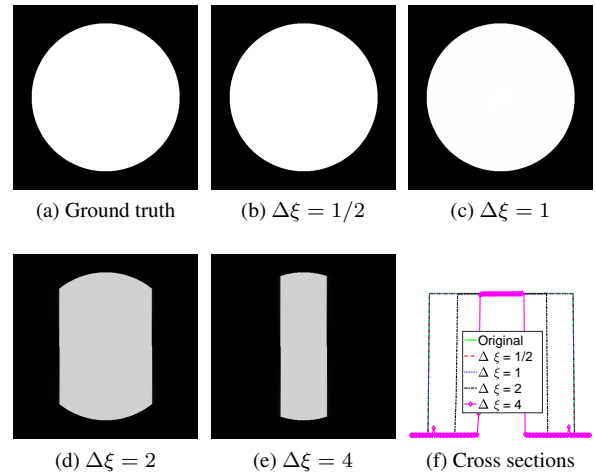


Figure 2: The sinc filtering effect with Cartesian sampling. Note: in that experiment, some ringing appears on the boundaries, explaining why the cropped images are darker.

of samples is equal to 153600, while the reference image contains  $512 \times 512$  pixels. Hence this experiment corresponds to a subsampling factor of 1.7. Notice that while the distance between consecutive samples is about 1 pixel in the  $k$ -space center, it reaches about 5 pixels in the outer part, meaning that the filtering effect will have a higher impact on high frequencies. Images of a brain phantom [14] were reconstructed using a standard nonlinear reconstruct-

tion algorithm described in Section 4.3.3. Fig. 4 shows the consequences of the integration and the sinc filtering on the images acquired with the spiral trajectory. When integration effects occur (Fig. 4b), the reconstructed image suffers from severe artifacts including a space varying blur, some contrast losses, a slight rotation (visible only by switching from one image to the next) and a modulation. In the case of bandlimiting filtering (Fig. 4c), the image quality degrades even more: a magnified region shows the loss of resolution as compared to the ground truth (Fig. 4a).

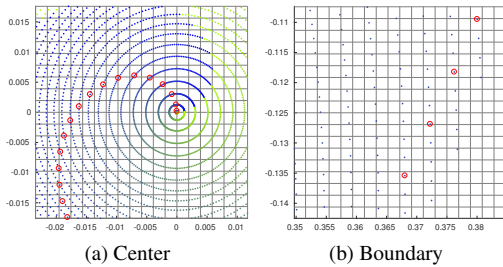


Figure 3: Two zooms on a sampling pattern made of 200 interleaved spirals. Each spiral has a different color.

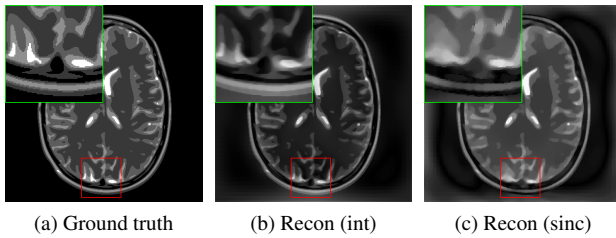


Figure 4: Example of reconstruction of an image sampled along the spirals of Fig. 3. The reconstruction algorithm does not account for the integration effect.

### 3 Validation of the filtering model

To the best of our knowledge, the forward model proposed in equation (2) has not been studied in the literature previously. The way the signal is digitized and processed depends on the MR receiver hardware, with specifications that are usually not transparent. In the following part, we therefore design a reverse-engineering technique to estimate the filter  $h$  and to validate the proposed model.

#### 3.1 A filter estimation procedure

We introduce a methodology to verify model (2) and to estimate the ADC filter. The principle reads as follows:

- Set a sampling period  $\delta t$ , a downsampling factor  $p \in \mathbb{N}$ , a number of measurements  $m \in p\mathbb{N}$  and a trajectory  $\lambda : [0, m\delta t] \rightarrow \mathbb{R}^2$ .
- Generate a first set of measurements  $\mathbf{y}_0 \in \mathbb{C}^m$  by sampling  $f = \hat{u} \circ \lambda$  with the rate  $\delta t$ .
- Generate a second set of measurements  $\mathbf{y}_1 \in \mathbb{C}^{m/p}$  by sampling  $f$  with the rate  $p\delta t$ .

In the case of an integrating ADC for instance, the noiseless measurements should then satisfy:

$$\mathbf{y}_1[i] = \sum_{j=0}^{p-1} \mathbf{y}_0[pi + j]. \quad (4)$$

A convenient way to express the model is  $\mathbf{y}_1 = \mathbf{h} \star \mathbf{y}_0 \downarrow p$ , where  $\star$  denotes the convolution product,  $\downarrow p$  is the downsampling by a factor  $p$  and  $\mathbf{h} = [1, \dots, 1]/p$  is a constant filter of size  $p$ . One way to verify equation (4) is then to solve the following optimization problem:

$$\min_{\mathbf{h} \in \mathbb{R}^m} \frac{1}{2} \|(\mathbf{h} \star \mathbf{y}_0 \downarrow p) - \mathbf{y}_1\|_2^2 + \frac{\alpha}{2} \|\mathbf{L}\mathbf{h}\|_2^2, \quad (5)$$

where  $\alpha \geq 0$  is a regularization parameter and  $\mathbf{L}$  is a regularizing operator. In all our experiments we set  $\mathbf{L}$  to be the discrete derivative and tune  $\alpha$  manually.

The underlying idea behind problem (5) is to find the best linear time invariant operator that allows to match the two sets of measurements  $\mathbf{y}_0$  and  $\mathbf{y}_1$ . The least square in equation (5) corresponds to a *deconvolution* problem, which is highly ill-posed [28]. Hence we propose to regularize it by adding a Tikhonov regularization. Problem (5) can easily be solved with an accelerated projected gradient descent. The interested reader is referred to the first paper on the subject [25].

**Remark 1.** In practice, the vector of measurements  $\mathbf{y}_0$  is itself filtered by the ADC and we can only expect this procedure to yield an estimation of the filter valid for the time resolution  $\delta t$  instead of  $m\delta t$ .

#### 3.2 The experimental setup

All acquisitions were performed on a 7-Tesla MR scanner (Siemens Healthineers, Erlangen, Germany) with a 1Tx/32Rx head coil (Nova Medical, Wilmington, MA, USA). To validate our model, an *ex vivo* baboon brain was imaged using a gradient recalled echo (GRE) sequence to

acquire the Cartesian and spiral data corresponding to the experiment described in the previous section 2.1.

We validated the model both for Cartesian and spiral sampling.

In the case of Cartesian sampling, we set  $\delta t = 10\mu s$  with a field-of-view (FOV) of  $20 \times 20 \text{ cm}^2$  for a target resolution of  $256 \times 256$ . We then designed three trajectories composed of 256 lines with different sampling periods  $\Delta t \in \{\delta t, 4\delta t, 16\delta t\}$ , i.e. in the framework of paragraph 3.1,  $p = 1, p = 4$  and  $p = 16$ . When considering a normalized FOV, those downsampling factors correspond to  $\Delta\xi = \frac{1}{4}, \Delta\xi = 1$  and  $\Delta\xi = 4$  respectively. For the case  $p = 4$ , we interleaved four sets of trajectories to fill the whole Cartesian grid, thus measuring enough information to reconstruct the image. Overall, the number of samples per line reached 1024, 256 and 256 for  $p = 1, p = 4$  and  $p = 16$  respectively.

In the case of spiral trajectories, we set  $\delta t = 5\mu s$  with the same field-of-view (FOV) of  $20 \times 20 \text{ cm}^2$ . Spirals were designed using the method proposed in [20] and were made of 20 shots for a target resolution of  $512 \times 512$ . In that experiment, we studied the cases  $p = 1, p = 2$  and  $p = 8$ . For the case  $p = 8$ , we interleaved 4 spirals to measure as much information as for  $p = 2$ . Overall, the number of samples per line reached 6144, 3072 and 3072 for  $p = 1, p = 2$  and  $p = 8$  respectively.

### 3.3 Filtering effects on experimental data

In order to validate the proposed model, we first reconstruct the images with Cartesian and spiral sampling using a simple conjugate gradient algorithm. The results are displayed in Fig. 5.

In the case of Cartesian trajectories, no filtering effects are observed for  $p = 1$  (Fig. 5a). For  $p = 4$ , corresponding to a sampling pattern at Shannon’s rate (i.e.  $\Delta\xi = 1$ ), two black bands appear at the top and bottom of the image (Fig. 5b). For the image on Fig. 5c corresponding to  $p = 16$  (i.e.  $\Delta\xi = 4$ ), four horizontal black bands can be observed and the object is cropped along the readout direction. This perfectly matches the effects described in Section 2.1 (Fig. 1 and 2). These results strongly suggest that the MR scanner applies a bandlimiting filter on the temporal signal. We will give further evidence of this observation in the next section.

In the case of spiral sampling, the image corresponding to  $p = 1$  on Fig. 5d is near perfectly resolved. For  $p = 2$ , the image gets slightly more blurry and the contrast is slightly deteriorated. For  $p = 8$ , the effect gets disastrous, with some parts of the image disappearing and strong rotational blurs.

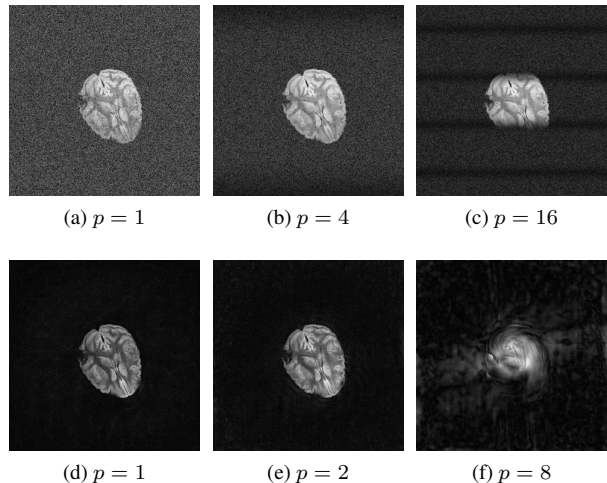


Figure 5: Direct reconstruction results of real data for the Cartesian trajectories (top) and spiral trajectories (bottom) with different sampling periods. Here we used a change of contrast to better highlight the effect.

### 3.4 Estimation of the filter

Problem (5) was solved to estimate the filter  $\mathbf{h}$  by using both Cartesian and spiral data. We solved the problem for each shot and channel independently and then averaged the result to reduce the noise. Fig. 6 shows the mean filter  $\mathbf{h}$  (red line) for the Cartesian and spiral experiments respectively. In both experiments, a sinc-like function can be identified, which supports that a near perfect bandlimiting filter is used on the ADC.

## 4 Handling the filtering effects in reconstruction algorithms

### 4.1 Discretizing the image

Let  $n \in 2\mathbb{N}$  denote a resolution parameter. In this paper, we assume that the true magnetization  $u$  can be written as:

$$u = u_d \star \psi, \quad (6)$$

where

$$u_d = \sum_{-n/2 \leq i, j < n/2} \mathbf{u}[i, j] \delta_{i/n, j/n} \quad (7)$$

is an atomic discretization of the image with  $\mathbf{u} \in \mathbb{C}^{n \times n}$  and  $\psi : [-\epsilon, \epsilon]^2 \rightarrow \mathbb{R}$  is a compactly supported interpolation kernel. The interest of this decomposition lies in the fact that it will allow using nonuniform fast Fourier transforms.

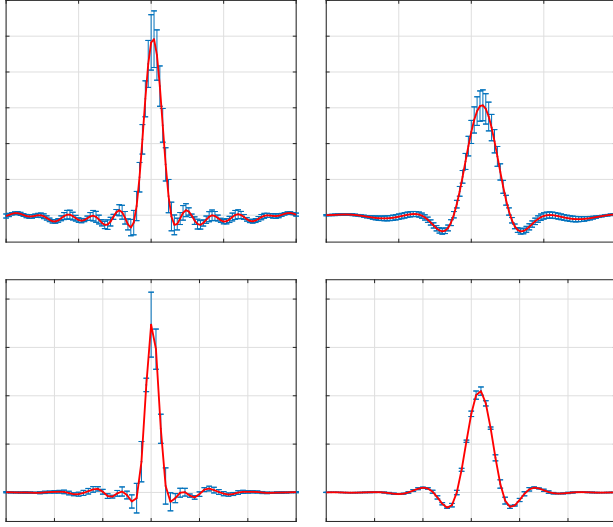


Figure 6: Mean and standard deviation for the estimated filters using the Cartesian data (top) and spiral data (bottom). For the Cartesian data, we used  $p = 4$  and  $p = 16$ . For the spiral data, we used  $p = 2$  and  $p = 8$ .

The simplest interpolation kernel  $\psi$  is the spline of order 0:

$$\psi(x, y) = \begin{cases} 1 & \text{if } -1/(2n) \leq x, y < 1/(2n), \\ 0 & \text{otherwise.} \end{cases}$$

It will be used in all the experiments of this paper.

**Remark 2.** Notice that the model (7) does not allow to reproduce any function  $u$ . An additional error term  $\Delta u : \Omega \rightarrow \mathbb{C}$  should be added for completeness. We can however show that this term can be bounded in  $L^p$  under regularity assumptions on  $u$ . We refer the interested reader to the following book for more details [10].

## 4.2 Fast implementation of the forward model

In order to reconstruct the image, nearly any reconstruction algorithm requires an implementation of the forward operator and its adjoint. In this section, we therefore propose a numerical algorithm to evaluate integrals of the form:

$$y_i = \int_{\mathbb{R}} h(i\Delta t - t) \hat{u}(\lambda(t)) dt. \quad (8)$$

It is based on a combination of numerical integration and of the nonuniform Fast Fourier transform.

### 4.2.1 The NFFT

The atomic structure in (7) allows using the non uniform Fast Fourier Transform (NFFT or NUFFT) [11, 16] to get a numerical expression of  $\hat{u}$  at a set of locations  $\mathbf{k} = (\mathbf{k}[0], \dots, \mathbf{k}[m-1]) \in \mathbb{R}^{m \times 2}$  in the  $k$ -space. We let  $\mathbf{k}_1$  and  $\mathbf{k}_2$  denote the two spatial components of  $\mathbf{k}$ . The NFFT allows evaluating rapidly with a high precision, all components of  $\hat{u}_d(\mathbf{k})$ , defined by:

$$\hat{u}_d(\mathbf{k}[l]) = \sum_{\substack{-n/2 \leq i < n/2 \\ -n/2 \leq j < n/2}} \mathbf{u}[i, j] \exp(-2i\pi(i\mathbf{k}_1[l] + j\mathbf{k}_2[l])). \quad (9)$$

While a naive implementation of the sum would require  $O(mn^4)$  operations, the NFFT reduces the complexity to  $O(n^2 \log(n) + m|\log(\epsilon)|^2)$ , where  $\epsilon$  is the desired precision. The constants involved in the  $O$  depend on the locations of the sampling points  $\mathbf{k}$ .

By using matrix-vector product notations, this can be rewritten as:

$$\hat{u}_d(\mathbf{k}) = \mathbf{N}_{\mathbf{k}}^* \mathbf{u},$$

where  $\mathbf{N}_{\mathbf{k}}^* \in \mathbb{C}^{m \times n^2}$  is the NFFT matrix. Then, to get the values of  $\hat{u}$ , we simply use the formula:  $\hat{u} = \hat{u}_d \odot \hat{\psi}$ . Overall, the mapping  $(\mathbf{u}, \mathbf{k}) \mapsto \hat{u}(\mathbf{k}) = \hat{\mathbf{u}}$  is given by:

$$\hat{\mathbf{u}} = \hat{\psi}(\mathbf{k}) \odot \mathbf{N}_{\mathbf{k}}^* \mathbf{u}.$$

**Remark 3.** When introducing the interpolating kernel  $\psi$ , we need to take special care of boundary conditions. The NFFT assumes periodic boundary conditions. In this work, we simply work with images surrounded by black, as is common in MRI, to avoid creating discontinuities on the boundaries.

### 4.2.2 Integration along the curve

In order to compute the integrals (8), we propose to use simple numerical integration procedures. Letting  $p \in \mathbb{N}$  denote an upsampling parameter, we shall use the following approximation:

$$y_i = (h \star f)(i\Delta t) \simeq \sum_{j \in \mathbb{Z}} h_j \cdot \hat{u}(\lambda(i\Delta t - j\delta t)), \quad (10)$$

where  $\delta t = \Delta t/p$  and where the weights  $h_j$  can be chosen either by using the estimation procedure proposed in Section 3.4 or taken equal to  $h(j\delta t)$  if an analytical version of  $h$  is available. More advanced Newton-Cotes formula [26] could also be used. The values  $\hat{u}(\lambda(i\Delta t - j\delta t))$  can be evaluated efficiently with the NFFT, and the weights  $h_j$  only need to be computed once at the start of the algorithm. In practice, we typically use values of  $p$  in the range  $\{1, \dots, 8\}$ .

The forward model  $\mathbf{A}$  can now be completely described. Letting  $\mathbf{k}$  denote the vector of discrete locations with components  $\mathbf{k}[i] = \lambda(i\delta t)$  for  $0 \leq i \leq mp - 1$ , it takes the following form:

$$\mathbf{A}\mathbf{u} = \mathbf{H}\Sigma_{\psi}\mathbf{N}_{\mathbf{k}}^*\mathbf{u},$$

where  $\mathbf{H}$  is the operator that computes the sums in equation (10) and where  $\Sigma_{\psi} : \mathbf{z} \mapsto \hat{\psi}(\mathbf{k}) \odot \mathbf{z}$ . The adjoint operator is given by:

$$\mathbf{A}^* = \mathbf{N}_{\mathbf{k}}\Sigma_{\psi}^*\mathbf{H}^*.$$

**Remark 4.** In the case of multiple coils, the forward model can be written as:

$$\mathbf{A}\mathbf{u} = \begin{pmatrix} \mathbf{H}\Sigma_{\psi}\mathbf{N}_{\mathbf{k}}^*\mathbf{S}_1\mathbf{u} \\ \vdots \\ \mathbf{H}\Sigma_{\psi}\mathbf{N}_{\mathbf{k}}^*\mathbf{S}_{n_c}\mathbf{u} \end{pmatrix},$$

where  $\mathbf{S}_k = \text{diag}(\mathbf{s}_k)$  is the diagonal matrix associated to the  $k$ -th sensitivity profile and  $n_c$  is the total number of receiver coils.

### 4.3 Reconstruction algorithms

Once the forward operator and its adjoint are properly described, most existing algorithms can be used out of the box. In this work, we implemented simple linear reconstructions based on the linear conjugate gradient method and more advanced nonlinear approaches. Other methods such as GRAPPA, SMASH, SENSE or ESPIRIT [17], could be easily modified to account for the integration too.

#### 4.3.1 Estimating the sensitivities

In all the experiments performed in this paper, we first acquire a reference image with a standard Cartesian trajectory sampled at twice Shannon's rate along the readout direction. This allows to simply estimate the sensitivities by using the sum-of-square approach [23].

#### 4.3.2 Linear reconstructions

One of the simplest ways to reconstruct an image is to solve the following Tikhonov-regularized least squares problem:

$$\min_{\mathbf{u} \in \mathbb{R}^n} \frac{1}{2} \|\mathbf{A}\mathbf{u} - \mathbf{y}\|_2^2 + \frac{\alpha}{2} \|\mathbf{u}\|_2^2.$$

The optimality conditions for this problem read

$$(\mathbf{A}^*\mathbf{A} + \alpha I)\mathbf{u} = \mathbf{A}^*\mathbf{y},$$

which can be solved with an iterative solver. In this paper, we simply use a linear conjugate gradient method [26].

#### 4.3.3 Nonlinear reconstructions

Nonlinear reconstructions are known to yield better results than linear ones, especially in the regime of subsampled data. The whole field of compressed sensing [21, 4], which under certain assumptions guarantees exact reconstructions, is based on  $\ell^1$ -regularized problems. In this paper, our nonlinear reconstructions are based on the resolution of the following problem:

$$\min_{\mathbf{u} \in \mathbb{R}^n} \frac{1}{2} \|\mathbf{A}\mathbf{u} - \mathbf{y}\|_2^2 + \alpha R(\mathbf{u}), \quad (11)$$

where  $R : \mathbb{C}^{n^2} \rightarrow \mathbb{R} \cup \{+\infty\}$  is a regularization term describing some prior information on the image that is sought for. This type of problem can be solved efficiently by using a Douglas-Rachford algorithm [8]. Letting  $f(\mathbf{u}) = \frac{1}{2} \|\mathbf{A}\mathbf{u} - \mathbf{y}\|_2^2$ , it reads as follows:

1. *Input:* initial guess  $\mathbf{v}_0 \in \mathbb{C}^{n^2}$  and parameter  $\gamma > 0$ .
2.  $\mathbf{u}_k = \text{Prox}_{\gamma f}(\mathbf{v}_k)$ .
3.  $\mathbf{v}_{k+1} = \mathbf{v}_k - \mathbf{u}_k + \text{Prox}_{\gamma \alpha R}(2\mathbf{u}_k - \mathbf{v}_k)$ .

The proximal operators  $\text{Prox}_{\gamma f}$  and  $\text{Prox}_{\gamma \alpha R}$  are defined by:

$$\text{Prox}_{\gamma f}(\mathbf{z}) = \arg \min_{\mathbf{u} \in \mathbb{C}^{n^2}} \frac{\gamma}{2} \|\mathbf{A}\mathbf{u} - \mathbf{y}\|_2^2 + \frac{1}{2} \|\mathbf{u} - \mathbf{z}\|_2^2 \quad (12)$$

and by

$$\text{Prox}_{\gamma \alpha R}(\mathbf{z}) = \arg \min_{\mathbf{u} \in \mathbb{C}^{n^2}} \gamma \alpha R(\mathbf{u}) + \frac{1}{2} \|\mathbf{u} - \mathbf{z}\|_2^2. \quad (13)$$

The step 2. above can be interpreted as the resolution of the inverse problem using Tikhonov regularization. It can be solved using a linear conjugate gradient algorithm. The step 3. can be interpreted as a *denoising* step. Depending on the prior  $R$ , different algorithms can be used. The sequence  $(\mathbf{u}_k)_{k \in \mathbb{N}}$  can be proved to converge to a global minimizer of (11) if  $R$  is a convex closed function with nonempty interior. In this work, we define  $R$  as the total variation of the image [5] and solve the proximal step (13) with the method proposed in [31].

**Remark 5.** Notice that total variation regularization is a simple prior leading to decent results, but suffering from some defects such as staircasing effect. More advanced denoising methods such as BM3D [9] image can be used instance, as was proposed in the plug-and-play-prior algorithm [29].



## 5 Reconstruction results

In this section, we will demonstrate how the proposed reconstruction algorithms perform on simulated and experimental data compared to traditional approaches.

### 5.1 Simulated data

We first consider the experiment of Section 2.2, in which the spiral sampling pattern of Fig. 3 was used to simulate measurements of a brain phantom incorporating the bandlimiting filtering with  $p = 2$ . Fig. 7b displays the brain phantom image reconstructed with the nonlinear algorithm of Section 4.3.3 that does not include the filtering in the forward model. Note that this corresponds to the standard MR reconstruction. We reconstructed the same data with the method proposed in Section 4, which accounts for the filtering effect. The result is displayed in Figure 7c. By looking at the magnified regions, we notice that the proposed reconstruction was able to recover the fine structural details present in the ground truth image (Fig. 7a), which had disappeared in the standard reconstruction (Fig. 7b).

**Remark 6.** *In all experiments, the regularization parameter  $\alpha$  of equation (11) was manually tuned so as to produce the best possible result. We had to take it larger for the standard model, otherwise, strong oscillations would have appeared in the reconstructed image, with no significant increase in the level of details.*

To further highlight the gain of resolution offered by the proposed approach, we repeated the same experiment with a synthetic image displayed in Figure 8. Here, we used another four-interleaved spiral which samples the  $k$ -space with a variable density decaying as the frequencies get higher. Images reconstructed with the standard method and the proposed approach are displayed in Figure 8a and 8b respectively. Notice how the resolution is enhanced by including the filtering effect in the forward model.

### 5.2 Experimental data

The proposed acquisition model and reconstruction schemes were tested on experimental data acquired from both spiral [20] and *sparkling* [3, 7, 19] sampling patterns.

#### 5.2.1 Spiral sampling

The spiral trajectory used for the acquisition was the same as in Section 3.3 for  $p = 8$ . The reconstruction results are displayed in Fig. 10. In this example, we simply used a linear reconstruction algorithm based on the conjugate

gradient since the subsampling factor was not large and 32 receiver channels were used. Even though the reconstruction accounting for the filtering effect is not perfect it is clearly far superior to a standard reconstruction.

#### 5.2.2 Sparkling sampling

The recently introduced Sparkling trajectories are novel non-Cartesian trajectories that produce optimal sampling patterns by taking full advantage of the hardware abilities [3, 7, 19].

**Remark 7.** *This project actually began thanks to these new trajectories. Our first attempts to use those trajectories led to unsatisfactory reconstruction results. We understood after long investigations that the main problem was related to the ADC filtering, which motivated us to write this paper. While the results presented for the spiral trajectory were mainly of tutorial value, since we artificially increased the sampling period  $\Delta t$ , the results presented in this paragraph are based on completely realistic data.*

The trajectory used in our experiments consisted of 128 shots composed of 512 samples each for a target resolution of  $512 \times 512$ , corresponding to a subsampling factor of 4. A typical trajectory is displayed in Fig. 9. Magnified regions of its center and periphery are displayed in Fig. 9b and 9c respectively. As can be seen, the distance between consecutive samples is larger than a pixel, be it in the central region or at the  $k$ -space boundary. These large gaps are related to the fact that the trajectory  $\lambda$  goes at the maximal speed offered by the hardware.

An *ex vivo* human brain was imaged and reconstructed with a standard nonlinear reconstruction algorithm and with the proposed method. The results are displayed in Fig. 11. Once again, the improvement of quality allowed by the proposed approach is striking, especially in the temporal lobes of the brain.

## 6 Discussion and Conclusion

In this work, we illustrated how the anti-aliasing filters implemented in analog-to-digital converters could be detrimental to the good reconstruction of MRI images. Depending on the speed of the trajectory and on the sampling period, these filters can have dramatic effects, with irreversible loss of information. To the best of our knowledge, these effects were ignored until now in the literature. We proposed novel numerical algorithms to mitigate them, yielding far superior reconstruction results than current approaches for some modern trajectories. This en-

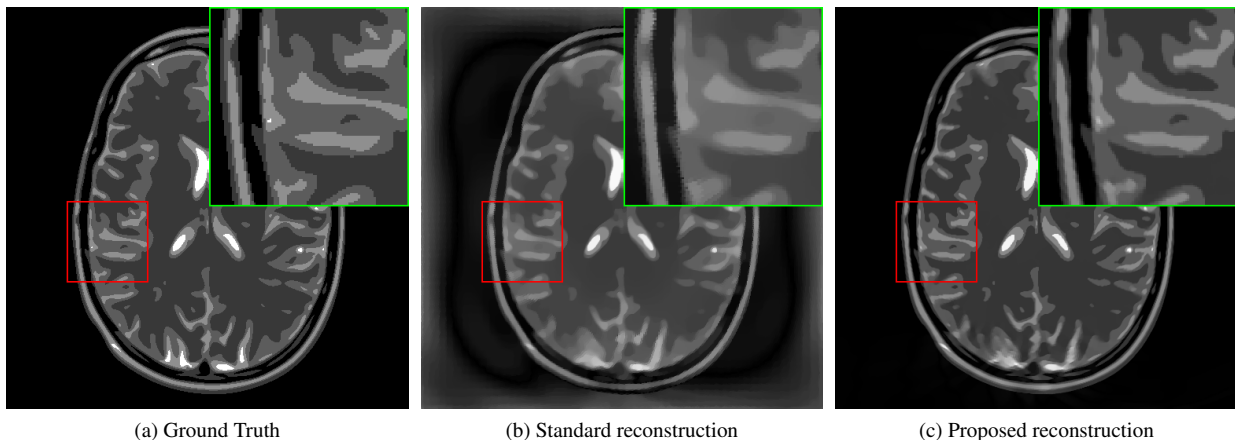


Figure 7: Reconstructions of the brain phantom image sampled along the spirals of Fig. 3 without (b) and with (a) accounting for the bandlimiting filtering effects.

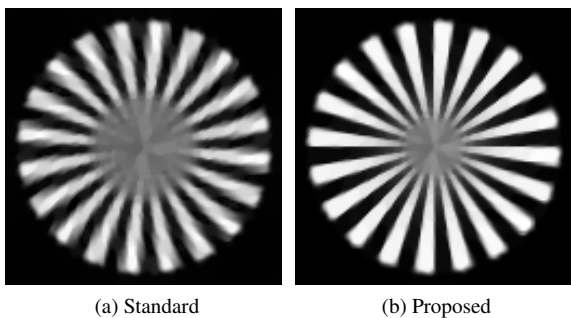


Figure 8: Reconstruction with and without the bandlimiting filtering accounted for.

hanced quality comes at the expense of a higher numerical complexity, with computing times typically multiplied by factors ranging from 2 to 4 compared to standard approaches.

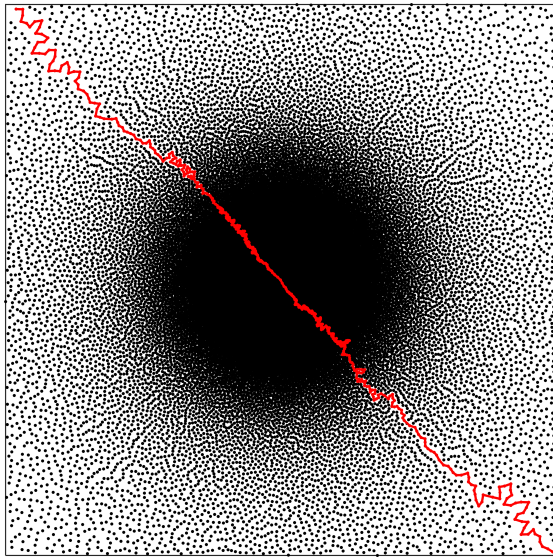
At this point, the reader may wonder why such anti-aliasing filters are actually implemented in practice. While they make perfect sense when the aim is to sample a purely temporal signal  $f(t) = \hat{u}(\lambda(t))$  using Shannon’s theory, their pertinence becomes less obvious when it comes to the reconstruction of spatial MR images  $u$ , especially with modern nonlinear reconstruction algorithms.

Let us consider their pros and cons. On the positive side, filtering allows to *reduce noise* and *increase the signal-to-noise-ratio*, which may sometimes be critical when little signal is available. In addition, it allows to *reduce the number of measurements* and hence leads to faster reconstruction algorithms. Those two arguments are probably the main ones explaining the very existence

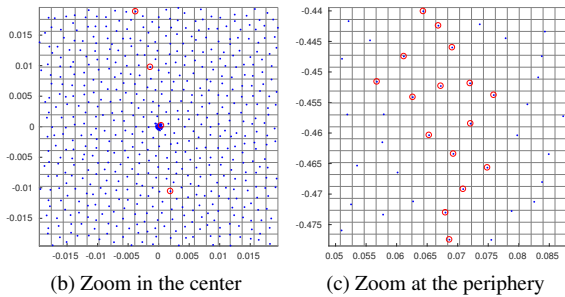
of these filters. In addition, it is physically impossible to measure pointwise values of  $f$ , and the filtering is an effect that cannot be avoided, up to the temporal resolution of the ADC. On the negative side, *applying filters trades temporal resolution for signal-to-noise-ratio*. It is however well known in the field of inverse problems that it is *much harder to gain resolution than signal-to-noise-ratio*. State-of-the-art denoisers are close to being unbeatable [6], while blurring induces an irreversible loss of information.

Overall, we believe that the increase of computational power using massively parallel architectures, makes the arguments supporting the filtering partly irrelevant. We hope that the current manuscript may motivate manufacturers to use or design different ADCs. For instance, a striking side-result of this work is that the older technology of integrating ADC is somewhat preferable to more complex bandlimiting ADCs, since the integrating filters do not cause an irreversible loss of information (compare Fig. 1 and Fig. 2). In addition, our analysis suggests to use *time-varying sampling periods*. In the center of the  $k$ -space, a lot of signal is usually available, allowing to use very short sampling periods. On the contrary, as the sampling trajectory gets more distant to the center, the sampling period should increase to account for the signal decay.

The key factor to know whether a trajectory is acceptable or not for standard reconstruction methods is the maximal distance between consecutive samples. Nearly no effect should be observed below half a pixel, slight effects will be observed between half a pixel and 1.5 pixels, and significant problems should appear beyond. The re-



(a) The whole trajectory



(b) Zoom in the center

(c) Zoom at the periphery

Figure 9: Sparkling trajectory and magnified regions of central and peripheral parts.

cent advances in sampling theory advocate the use of more complex trajectories with high speeds [30, 22, 1, 19] that may cross the critical regime of sampling distances. All those arguments make us believe that the proposed analysis and algorithmic framework may play an important role in the future.

**Acknowledgements** C. Lazarus and P. Weiss wish to acknowledge P. Ciuciu and A. Vignaud for helping them to identify the filtering effect thanks to their strong engagement in the acquisition of Sparkling sampling patterns. M. März and P. Weiss wish to warmly thank G. Kutyniok for her support and enabling them to meet on a regular basis.

We would like to express our gratitude to the donors involved in the body donation program of the *Association des dons du corps du Centre Ouest*, Tours, who made it possible to use an *ex vivo* human brain as phantom for our experiments, by generously donating their bodies for science. We also would like to acknowledge C. Destrieux

and I. Zemmoura for the extraction and fixation of this anatomical piece. We also wish to thank M. Bottlaender for provided the baboon phantom.

C. Lazarus wishes to thank the CEA Irtelis international PhD program for its financial support. She also acknowledges the France Life Imaging project Multi-CS-MRI, which supported her travelling expenses to ITAV. M. März is supported by the DFG Priority Programme DFG-SPP 1798. P. Weiss thanks the ANR JCJC OMS for partial funding.

## References

- [1] C. B. Ahn, J. H. Kim, and Z. H. Cho. High-Speed Spiral-Scan Echo Planar NMR Imaging-I. *IEEE Transactions on Medical Imaging*, 5(1):2–7, 1986.
- [2] R. Ansorge and M. J. Graves. *The Physics and Mathematics of MRI*. Morgan & Claypool Publishers, 2016.
- [3] C. Boyer, N. Chauffert, P. Ciuciu, J. Kahn, and P. Weiss. On the Generation of Sampling Schemes for Magnetic Resonance Imaging. *SIAM Journal on Imaging Sciences*, 9(4):2039–2072, 2016.
- [4] E. J. Candès, J. Romberg, and T. Tao. Robust uncertainty principles: exact signal reconstruction from highly incomplete frequency information. *IEEE Transactions on information theory*, 52(2):489–509, 2006.
- [5] A. Chambolle, V. Caselles, D. Cremers, M. Novaga, and T. Pock. An introduction to total variation for image analysis. *Theoretical Foundations and Numerical Methods for Sparse Recovery*, 9(263-340):227, 2010.
- [6] P. Chatterjee and P. Milanfar. Is Denoising Dead? *IEEE Transactions on Image Processing*, 19(4):895–911, 2010.
- [7] N. Chauffert, P. Ciuciu, J. Kahn, and P. Weiss. A Projection Method on Measures Sets. *Constructive Approximation*, 45(1):83–111, 2017.
- [8] P. L. Combettes and J.-C. Pesquet. Proximal Splitting Methods in Signal Processing. In *Fixed-Point Algorithms for Inverse Problems in Science and Engineering*, pages 185–212. Springer, 2011.
- [9] K. Dabov, A. Foi, V. Katkovnik, and K. Egiazarian. Image denoising by sparse 3D transform-domain collaborative filtering. *IEEE Transactions on Image Processing*, 16(8):2080–2095, 2007.

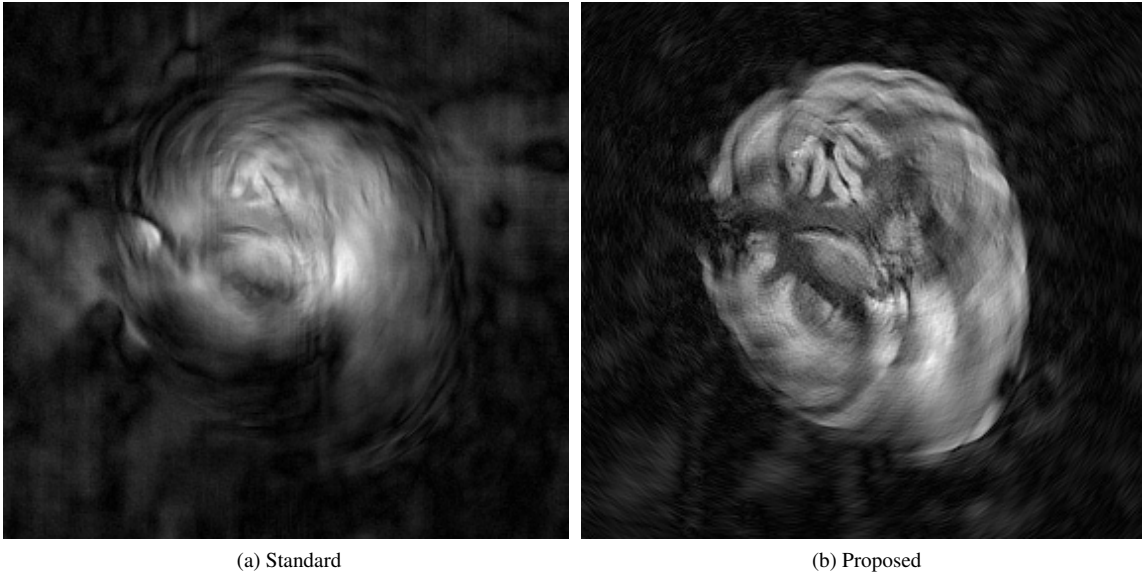


Figure 10: Linear reconstructions of an *ex vivo* baboon brain acquired with a spiral trajectory, with (a) and without (b) the bandlimiting filtering accounted for. Acquisitions were prospectively performed on a 7 Tesla MR scanner.

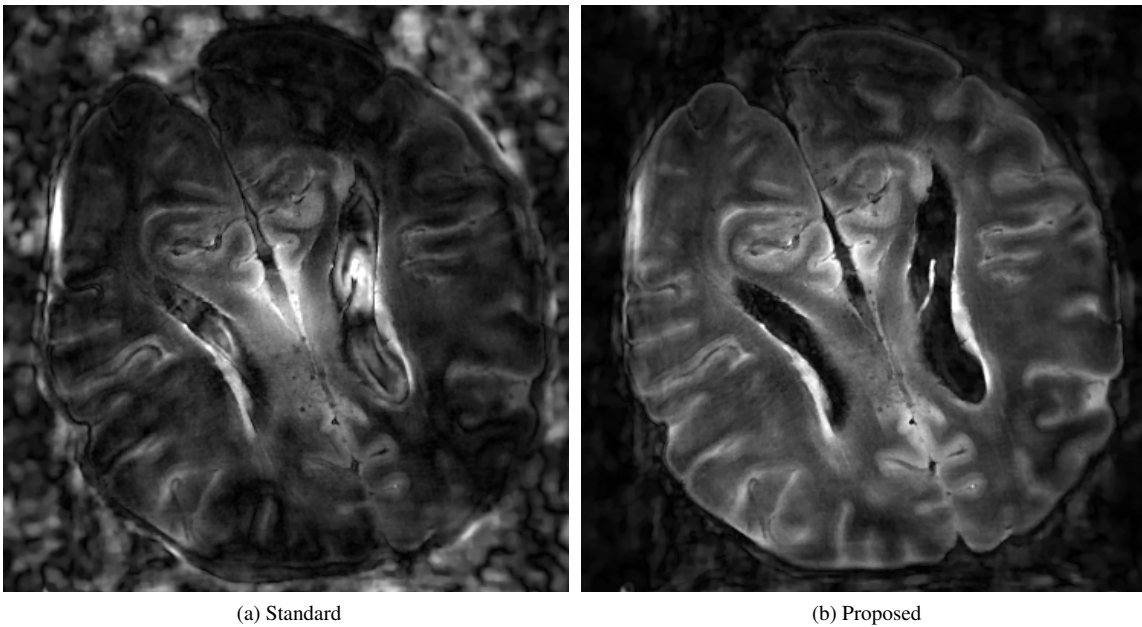


Figure 11: Nonlinear reconstructions of *ex vivo* human brain with a Sparkling trajectory, with (a) and without (b) the bandlimiting filtering accounted for. Acquisitions were prospectively performed on a 7 Tesla MR scanner.

- [10] R. A. DeVore and G. G. Lorentz. *Constructive Approximation*. Springer-Verlag Berlin Heidelberg, 1993.
- [11] A. Dutt and V. Rokhlin. Fast Fourier Transforms for Nonequispaced Data. *SIAM Journal on Scientific computing*, 14(6):1368–1393, 1993.
- [12] J. A. Fessler. Model-Based Image Reconstruction for MRI. *IEEE Signal Processing Magazine*, 27(4):81–89, 2010.
- [13] J. Graessner. Bandwidth in MRI. *Magnetom Flash*, 2:3–8, 2013.
- [14] M. Guerquin-Kern, L. Lejeune, K. P. Pruessmann, and M. Unser. Realistic analytical phantoms for parallel magnetic resonance imaging. *IEEE Transactions on Medical Imaging*, 31(3):626–636, 2012.
- [15] D. I. Hoult. The nmr receiver: A description and analysis of design. *Progress in Nuclear Magnetic Resonance Spectroscopy*, 12(1):41–77, 1978.
- [16] J. Keiner, S. Kunis, and D. Potts. Using NFFT 3—A Software Library for Various Nonequispaced Fast Fourier Transforms. *ACM Transactions on Mathematical Software (TOMS)*, 36(4):19, 2009.
- [17] D. J. Larkman and R. G. Nunes. Parallel magnetic resonance imaging. *Physics in Medicine & Biology*, 52(7):R15, 2007.
- [18] P. C. Lauterbur. *Image Formation by Induced Local Interactions: Examples Employing Nuclear Magnetic Resonance*. Nature Publishing Group, 1973.
- [19] C. Lazarus, P. Weiss, N. Chauffert, F. Mauconduit, M. Bottlaender, A. Vignaud, and P. Ciuciu. SPARKLING: Novel Non-Cartesian Sampling Schemes for Accelerated 2D Anatomical Imaging at 7T Using Compressed Sensing. In *25th annual meeting of the International Society for Magnetic Resonance Imaging*, 2017.
- [20] J. H. Lee, B. A. Hargreaves, B. S. Hu, and D. G. Nishimura. Fast 3D imaging using variable-density spiral trajectories with applications to limb perfusion. *Magnetic Resonance in Medicine*, 50(6):1276–1285, 2003.
- [21] M. Lustig, D. Donoho, and J. M. Pauly. Sparse MRI: The application of compressed sensing for rapid MR imaging. *Magnetic Resonance in Medicine*, 58(6):1182–1195, 2007.
- [22] P. Mansfield. Multi-planar image formation using NMR spin echoes. *Journal of Physics C: Solid State Physics*, 10(3), 1977.
- [23] C. A. McKenzie, E. N. Yeh, M. A. Ohliger, M. D. Price, and D. K. Sodickson. Self-calibrating parallel imaging with automatic coil sensitivity extraction. *Magnetic Resonance in Medicine*, 47(3):529–538, 2002.
- [24] C. H. Meyer, B. S. Hu, D. G. Nishimura, and A. Macovski. Fast spiral coronary artery imaging. *Magnetic Resonance in Medicine*, 28(2):202–213, 1992.
- [25] Y. Nesterov. Smooth minimization of non-smooth functions. *Mathematical Programming*, 103(1):127–152, 2005.
- [26] A. Ralston and P. Rabinowitz. *A First Course in Numerical Analysis*. Courier Corporation, 2001.
- [27] CE Shannon. A Mathematical Theory of Communication. *The Bell System Technical Journal*, 27(3):379–423, 1948.
- [28] A. Tarantola. *Inverse Problem Theory and Methods for Model Parameter Estimation*, volume 89. SIAM, 2005.
- [29] S. V. Venkatakrisnan, C. A. Bouman, and B. Wohlberg. Plug-and-Play priors for model based reconstruction. In *Global Conference on Signal and Information Processing (GlobalSIP) IEEE*, pages 945–948, 2013.
- [30] M. Weiger, J. Overweg, M. B. Rösler, R. Froidevaux, F. Hennel, B. J. Wilm, A. Penn, U. Sturzenegger, W. Schuth, M. Mathlener, et al. A high-performance gradient insert for rapid and short-T2 imaging at full duty cycle. *Magnetic Resonance in Medicine*, 2017.
- [31] P. Weiss, L. Blanc-Féraud, and G. Aubert. Efficient Schemes for Total Variation Minimization Under Constraints in Image Processing. *SIAM Journal on Scientific Computing*, 31(3):2047–2080, 2009.